Observing and Modeling Short-Term Changes in Basal Friction During Rain-Induced Speed-Ups on an Alpine Glacier

Anuar Togaibekov, Florent Gimbert, Adrien Gilbert, Andrea Walpersdorf

Geophysical Research Letters

RESEARCH LETTER
10.1029/2023GL107999

Observing and Modeling Short-Term Changes in Basal Friction During Rain-Induced Speed-Ups on an Alpine Glacier

Anuar Togaibekov[1,2], Florent Gimbert[2], Adrien Gilbert[2], and Andrea Walpersdorf[1]

[1]University of Grenoble Alpes, CNRS, IRD, UGE, ISTerre, Grenoble, France, [2]University of Grenoble Alpes, CNRS, IRD, IGE, Grenoble, France

Key Points:

- With Global Positioning System we observe rain-induced glacier speed-up events associated with surface uplift and down-glacier migration
- Observations and modeling show that water pressure rather than cavity size mainly controls changes in basal friction during these events
- We propose a generalized version of the "regularized" Coulomb friction law, adapted to transient friction under rapid water pressure variations

Supporting Information:

Supporting Information may be found in the online version of this article.

Correspondence to:

A. Togaibekov,
anuar.togaibekov@univ-grenoble-alpes.fr

Citation:

Togaibekov, A., Gimbert, F., Gilbert, A., & Walpersdorf, A. (2024). Observing and modeling short-term changes in basal friction during rain-induced speed-ups on an Alpine glacier. *Geophysical Research Letters*, *51*, e2023GL107999. https://doi.org/10.1029/2023GL107999

Received 5 JAN 2024
Accepted 6 JUN 2024

Abstract Basal shear stress on hard-bedded glaciers results from normal stress against bed roughness, which depends on basal water pressure and cavity size. These quantities are related in a steady state but are expected to behave differently under rapid changes in water input, which may lead to a transient frictional response not captured by existing friction laws. Here, we investigate transient friction using Global Positioning System vertical displacement and horizontal velocity observations, basal water pressure measurements, and cavitation model predictions during rain-induced speed-up events at Glacier d'Argentière, French Alps. We observe up to a threefold increase in horizontal surface velocity, spatially migrating at rates consistent with subglacial flow drainage, and associated with surface uplift and increased water pressure. We show that frictional changes are mainly driven by changes in water pressure at nearly constant cavity size. We propose a generalized friction law capable of capturing observations in both the transient and steady-state regimes.

Plain Language Summary Changes in water input at the bed of glaciers greatly modify their sliding speed by changing subglacial water pressure. High water pressure, induced by extreme meltwater input, is thought to increase cavity size, a process known as cavitation, which reduces direct contact and increases basal sliding speed. Our Global Positioning System observations indicate that the existing cavitation law, which is based on multidecadal sliding velocities of an alpine glacier, fails at capturing short-lived, rain-induced speed-ups. This is because cavities have insufficient time to adjust their size in response to water pressure changes. Here, we propose a generic friction law that satisfyingly captures observations by incorporating a direct dependency of basal friction on water pressure.

1. Introduction

Our current understanding of the physics of glacier basal sliding mainly relies on the seminal work of Weertman (1957) and Lliboutry (1958). Weertman proposed a sliding theory that describes ice motion over a rough, non-deformable bed via ice regelation and enhanced creep from stress concentrations around bedrock bumps (Kamb, 1970; Nye, 1969, 1970; Weertman, 1957). Lliboutry added to this theory the possibility that water cavities can form in the lee of bedrock bumps, such that water reaching the bed may change cavity size, thus reducing the apparent bed roughness, facilitating ice creep and causing faster sliding (Fowler, 1986, 1987; Gagliardini et al., 2007; Iken, 1981; Lliboutry, 1968; Schoof, 2005).

A wealth of theoretical studies established physically based sliding laws under Weertman and Lliboutry principles. These laws formulate bed shear stress τ_b as a function of glacier basal velocity U_b and basal effective pressure N, where N represents ice pressure minus water pressure (de Diego et al., 2022; Fowler, 1986; Gagliardini et al., 2007; Schoof, 2005). In all these laws, the basal effective pressure is assumed to be in equilibrium with the cavity geometry, such that τ_b can be equivalently expressed as a function of U_b and N (Gagliardini et al., 2007; Schoof, 2005), or U_b and a cavitation geometrical parameter θ (Gilbert et al., 2022; Thøgersen et al., 2019), or a wetted area A_0 (Tsai et al., 2022). Although this assumption appears to be reasonable under a scenario where cavity or subglacial geometry has sufficient time to adjust to changes in pressure (Gimbert et al., 2021), its applicability for shorter timescales is questionable. At shorter timescales, water pressure may vary more rapidly than cavity geometry, such that water pressure alone (without cavity geometry change) may affect sliding speed by modifying interfacial stresses in cavitated parts of the bed, thus altering the force balance at the ice-bed interface (Iken, 1981; Schoof, 2005). In this case, a more complete friction law would describe τ_b as a function of all three variables U_b, N, and θ (Iken, 1981). However, such a law has not yet been proposed, and the

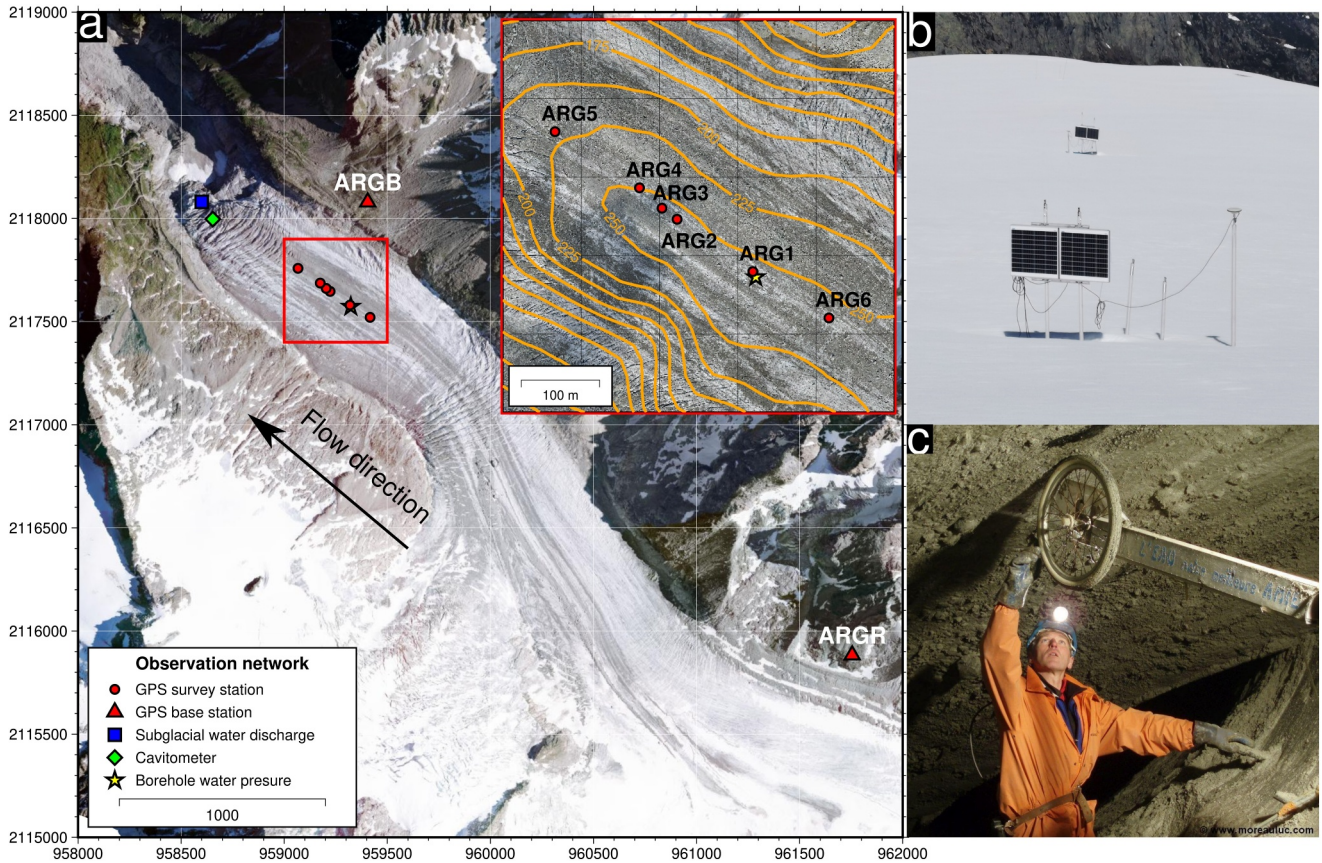

Figure 1. (a) Map showing the observation network at the Glacier d'Argentière. The red rectangle indicates the location of the six along-flow Global Positioning System (GPS) sites (red circles, also shown in the top-right inset map). The isolines in this inset show the glacier thickness in meters. Coordinates are given in the cartesian NTF (Paris)/Lambert zone II coordinate system. (b, c) Pictures of (b) two GPS stations and (c) the cavitometer.

extent to which its development is necessary in order to capture short-term glacier sliding changes under real configurations remains to be investigated. This is the primary objective of the present study.

While the link between sliding speed and water pressure under transient scenarios is generally well established (Das et al., 2008; Fudge et al., 2009; Harper et al., 2007; Iken, 1981; Sugiyama & Gudmundsson, 2004), it remains uncertain whether this relationship occurs mainly through pressure-driven changes in cavitation θ or force balance at the ice-bed interface. This uncertainty arises because surface uplift measurements, used to evaluate changes in cavitation, are uncertain, as they are influenced not only by variations in bed separation but also by spatial changes in glacier flow causing compression- and/or extension-induced changes in surface elevation (Hooke et al., 1989; Howat et al., 2008; Mair et al., 2002; Sugiyama & Gudmundsson, 2004; Vincent et al., 2022). In addition, separating the contribution of cavitation from that of force balance on basal sliding speeds requires the use of an empirical law linking cavitation and basal sliding speeds that is well-constrained from independent observations.

In this study, we investigate the velocity changes associated with rain events at the Glacier d'Argentière in the French Alps. By combining observational and modeling strategies, we dissociate the control of pressure-driven changes in force balance from that of pressure-driven changes in cavitation and propose a friction law adapted to rapid water pressure variations.

2. Data and Methods

2.1. The Glacier d'Argentière

The Glacier d'Argentière is situated in the Mont-Blanc massif in the French Alps (Figure 1a) and is known to be a hard-bedded glacier (Vincent & Moreau, 2016; Vivian & Bocquet, 1973). It initiates at about 3,400 m a.s.l. and

terminates at around 1,600 m a.s.l., spanning a total length of ∼10 km. The equilibrium-line altitude lay at about 2,900 m in 2019–2021. Our study site is located in the ablation zone at ∼2,380 m where the glacier has a relatively shallow sloping (10% surface slope) and a maximum thickness of 250 m (Figure 1a). At this location, the average melt rate from May to September is 0.04 m d^{-1}.

2.2. The Field Instrumentation

2.2.1. GPS Positioning

We use six Global Positioning System (GPS) stations along the glacier's central-flow line, with five (ARG1 to ARG5) deployed in February 2019 and the sixth (ARG6) in February 2020 (see inset map in Figure 1a). The GPS antennas are mounted on aluminum masts anchored up to 6 m deep in the ice (Figure 1b). We process GPS phase observables sampled at Δt of 30 s in kinematic mode using the TRACK software (Chen, 1999; Herring et al., 2018) with respect to the reference station ARGR, located about 3 km up-glacier on bedrock (Figure 1a). The position estimates yield an average root-mean-square (RMS) error of ±5.4 mm and ±7.7 mm for horizontal and vertical coordinates, respectively (Text S1 and Figure S1 in Supporting Information S1). The associated RMS of horizontal velocity is 0.4 mm hr^{-1}. To be conservative, we do not interpret ice velocities below 1 mm hr^{-1} (Text S1 and Figure S2 in Supporting Information S1). Vertical displacements are calculated separately for each period of interest due to frequent discontinuities caused by antenna height change. To focus on short-term variability instead of longer-term seasonal trends (Text S4 in Supporting Information S1), we remove a seasonally controlled linear trend in the vertical displacement time series and impose a common reference at an arbitrary datum. In Section 3.1, we present averaged time series data over all GPS stations.

We calculate uplift from vertical strain ΔZ by assuming a homogeneous vertical strain rate with depth H and ice incompressibility, in which case we have:

$$\Delta Z = \frac{\Delta U}{\Delta L} H \Delta t \tag{1}$$

with $\Delta t = 30$ s and $\Delta U/\Delta L$ is the horizontal strain rate, calculated as the spatial derivative of horizontal velocity U as measured over the along-flow distance L separating ARG1 (or ARG6 from 2020 on) from ARG5. Similar to the approach used for observed vertical displacements, we remove the linear trend from the vertical strain data and impose a common reference at an arbitrary datum.

2.2.2. Complementary Observations

In addition to GPS, we utilize a wide range of complementary observations. In-situ measurements of basal sliding velocity are made thanks to direct access to a subglacial cavity and the installation of specialized equipment known as a "cavitometer" (Figure 1c and green diamond in Figure 1a) (Gimbert et al., 2021; Vivian & Bocquet, 1973). Water discharge (blue square in Figure 1a) is recorded in excavated tunnels below the glacier tongue (a few hundred meters below the cavitometer) at a 15-min time step, with a discharge threshold of approximately 10 m^3 s^{-1} due to collector capacity limitations (Vincent & Moreau, 2016). The water predominantly exits through a well-identified notch in the bedrock valley, with only a minimal amount of water flowing out elsewhere. Water pressure is measured in a borehole (yellow star in Figure 1a) reaching the glacier bed, using a piezometer positioned 95 m above the bed. To obtain the basal water pressure, we add a constant pressure equivalent to the water column height of 95 m. Liquid precipitation data are obtained at 30-min intervals from the SAFRAN reanalysis (Vernay et al., 2022).

2.3. Model Description

The multidecadal measurements of basal sliding velocity and water discharge on the Glacier d'Argentière have allowed to establish a calibrated cavitation law that is observationally constrained and captures sliding velocity changes that occurred over the past decades (Gilbert et al., 2022; Gimbert et al., 2021). In the model of Gilbert et al. (2022), basal friction and subglacial hydrology are coupled through the transient evolution of the cavitation ratio θ as:

$$\tau_b^m = (1-\theta)\frac{U_b}{A_s} \tag{2}$$

where A_s is the Weertman friction coefficient (m a^{-1} MPa^{-m}), m is an exponent, and U_b is the basal sliding velocity. The evolution of θ through time is computed as a function of effective pressure N and sliding velocity U_b through the evolution equation:

$$\frac{d\theta}{dt} = \frac{1}{l_r}\left(U_b(1-\theta)^{\frac{1}{q}} - A_s C^m |N|^{m-1} N \left(\frac{\theta}{\alpha}\right)^{\frac{1}{q}}\right) \tag{3}$$

where l_r is a characteristic length scale (m) representative of a distance between bedrock bumps, C, q, and α are positive constants as defined in Gagliardini et al. (2007). Following Gilbert et al. (2022), we solve the model in a slab configuration with geometry adapted to our study site, setting the basal slope to 3° and τ_b equals 0.1 MPa as in numerical inversions (Gilbert et al., 2023). We use similar parameter values as constrained from long-term observations in Gilbert et al. (2022) except for m and A_s, and l_r. $m = 3$ is used as a glacier-wide representative value (Gilbert et al., 2023). A_s is inferred by fitting the basal sliding velocity time series obtained by subtracting a constant deformation velocity U_d from GPS-measured surface velocities, with $U_d = 25 \pm 5$ m a^{-1} based on numerical inversions (Gilbert et al., 2023). The value of $l_r = 1.0$ m has been adjusted to match the observed amplitude of vertical displacement associated with the rain events. In this study, we use this calibrated model as a reference for changes in basal sliding velocity U_b occurring solely through changes in cavitation ratio θ. This enables us to test whether an additional contribution from changes in effective pressure is required.

3. Results

3.1. Generic Features of Speed-Up Events

We observe nine distinctive speed-up events induced by intense rainfall over the 3-year period 2019–2021 (Figure 2, Figures S3 and S4 in Supporting Information S1). Three of these events occur during the early ablation period (May and early June) and six during the late ablation period (late August, September, and October). No events occur during the high-discharge period, which spans most of the summer from mid-June to late August (Figure S5b in Supporting Information S1). Horizontal velocity (red curve in Figure 2b) and water discharge (dark blue curve in Figure 2c) typically increase by a factor of about 2–3 with respect to the background level, and uplift (gray curve in Figure 2c) ranges from 0.02 to 0.07 m. These events are also visible in the basal speed record from the cavitometer (green curve in Figure 2b).

Interestingly, we observe differences in phasing and durations across the various measured variables. Subglacial water discharge and horizontal velocity increase nearly immediately after rainwater input (dashed vertical line in Figures 2a–2c), suggesting that water is efficiently drained from the surface to the glacier base. This pattern is also observed in all nine speed-up events (Text S2 in Supporting Information S1). Horizontal velocity, however, starts to rise before water pressure (light blue curve in Figure 2b) and reaches a maximum (dotted vertical line in Figures 2a–2c) before water discharge but concomitantly with water pressure (events 1, 2, and 4). After this maximum, both horizontal velocity and water pressure decrease, while water discharge remains elevated. Horizontal velocity returns to the pre-event value, while water pressure decreases significantly below, which we interpret as a local effect (see Section 4.2). We note that the timing of the basal speed records from the cavitometer closely matches that of the GPS, suggesting that changes in glacier surface velocity during speed-up events are predominantly due to changes in sliding velocity. Vertical displacement and water discharge reach maximum levels at approximately the same time, slightly after maximum horizontal velocity, and persist for similar durations, typically of a few days. We also note the presence of horizontal velocity oscillations before and after event 2 (Figure 2b), for which no clear trigger could be identified, although they are likely related to melting events (Text S3 in Supporting Information S1).

During times of elevated basal water pressure (greater than the background value of 16 bar), we observe a nonlinear relationship between horizontal velocity and basal water pressure for autumn events 1–3 (Figure 2d). Spring event 4 falls out of that relationship, likely as a result of subglacial hydrology conditions being different at this time (Section 4.2). Meanwhile, vertical displacement exhibits a strong dependency on water discharge (up to

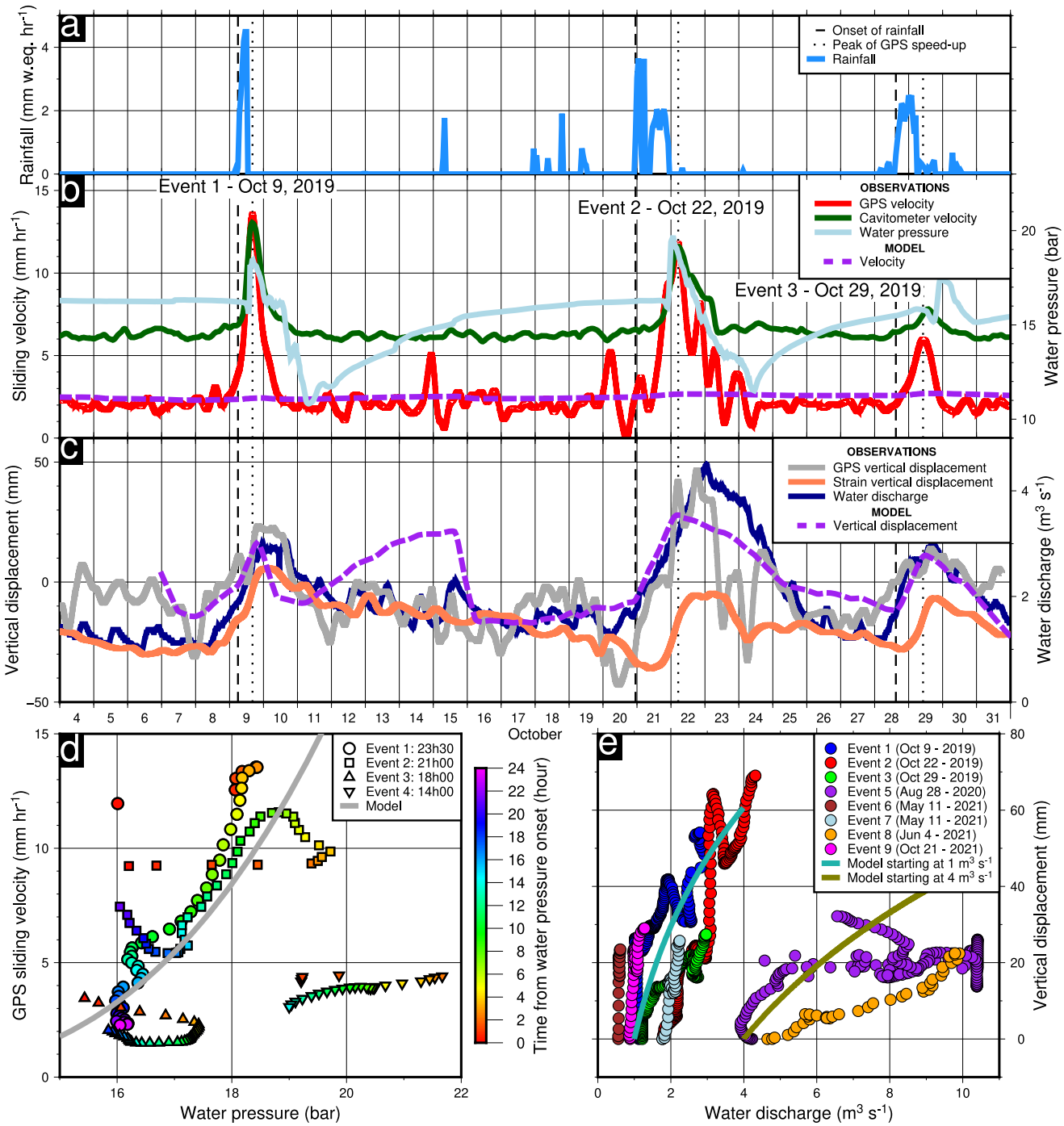

Figure 2. Relationship between GPS-derived sliding velocity measurements averaged over the five stations and other observations. Temporal variations in October 2019 in panels (a) liquid precipitation; (b) Global Positioning System (GPS), cavitometer, and modeled sliding velocity; (c) GPS, strain-induced, and modeled vertical displacement and observed water discharge. The plot for events 4–9 is available in Text S2 in Supporting Information S1 (Figure S3 in Supporting Information S1). The vertical dashed lines in panels (a, b, c) mark the onset of the rainfall events, and the dotted lines mark the peak horizontal velocity associated with each event. Panels (d–e) show the observed and modeled relationship between (d) water pressure and GPS-derived sliding velocity, and (e) water discharge and vertical displacement. In panel (d), water pressure is shown only when it exceeds the background level.

60 mm uplift for a 2 $m^3 s^{-1}$ change) when pre-event water discharge is low (<2 $m^3 s^{-1}$, events 1–3, 6, 7, 9) but a weak dependency (up to 20 mm uplift for a 6 $m^3 s^{-1}$ change) when pre-event water discharge is high (>2 $m^3 s^{-1}$, events 4, 5, 8). We estimate that the contribution of basal uplift on vertical displacement is significant since

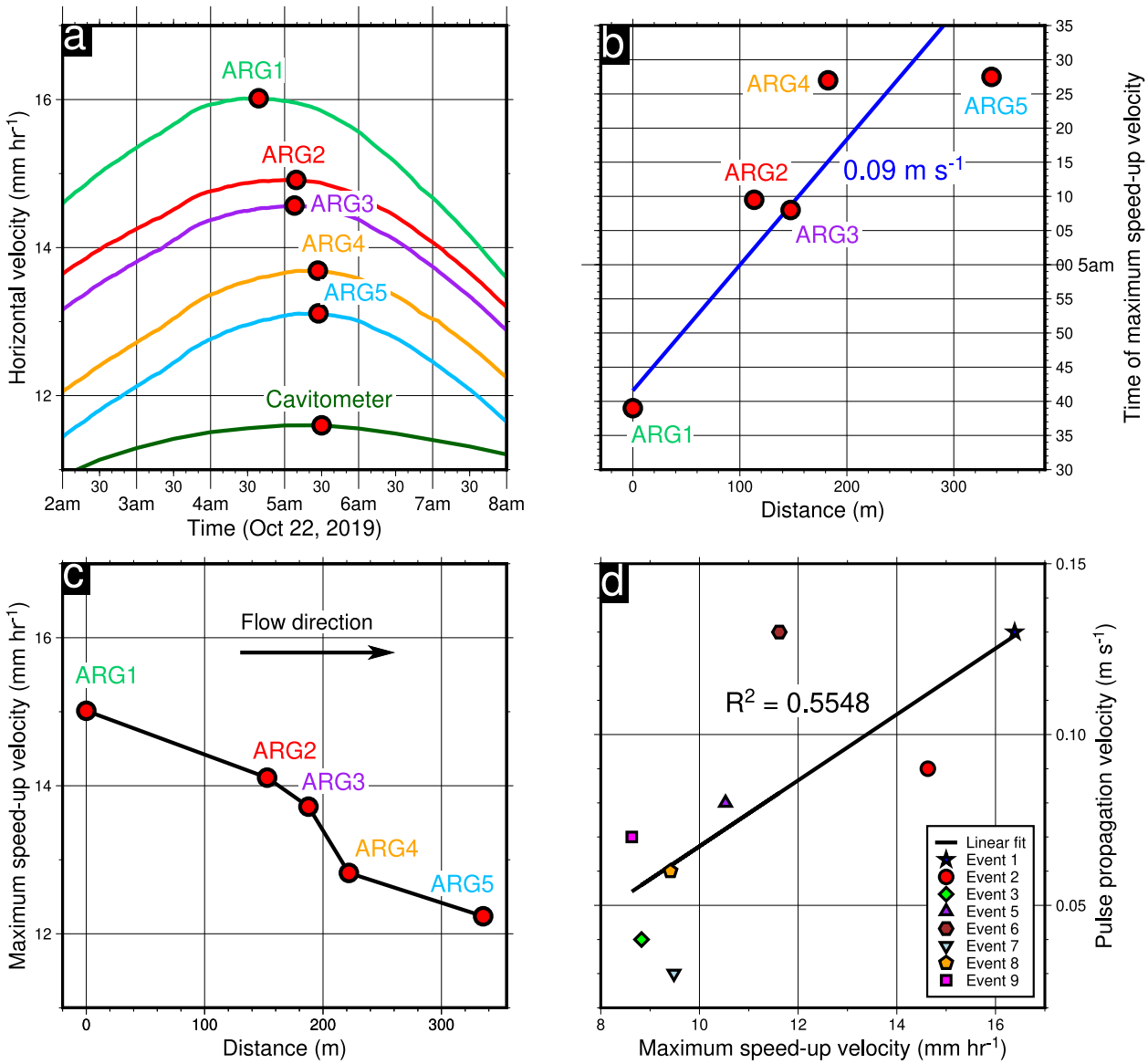

Figure 3. (a) Horizontal velocity as a function of time for five Global Positioning System (GPS) sites and the cavitometer. (b) Time of maximum speed-up velocity as a function of distance along flow, ARG1 being the reference. (c) Maximum speed-up velocity as a function of distance between GPS stations as in panel (b). Subfigures (a–c) present results for event 2, and the other events are shown in Text S4 in Supporting Information S1 (Figures S7–S9 in Supporting Information S1). (d) Pulse propagation velocity as a function of maximum horizontal velocity (averaged over the central transect GPS sites). Note that event 4 is excluded due to pulse propagation not being observed.

surface uplift due to strain rate (orange curve in Figure 2c) ranges between 0.01 and 0.04 m, which for most events is about half the total observed uplift.

3.2. Pulse Propagation Velocity as a Proxy of Subglacial Flow Propagation

By comparing the velocity signal at the different GPS stations, we observe a specific pattern in the amplitude and phasing of speed-up events. The highest peak velocity occurs at the uppermost station (ARG1 in 2019 and ARG6 in 2021–2022) and the amplitude typically decreases down-glacier in the flow direction for the rest of the central GPS sites (Figure 3c and Figure S7 in Supporting Information S1). This finding is consistent with lower velocity changes occurring at the cavitometer site located much further down-glacier compared to GPS sites. Moreover, maximum velocity generally occurs in chronological order from uppermost to lowermost locations (Figure 3a and Figure S8 in Supporting Information S1), showing that speed-up propagates along the flow. We determine the

speed-up along-flow migration velocity by linearly fitting the time of peak velocity against distance along the central transect of GPS sites ARG1-5 (Figure 3b and Figure S9 in Supporting Information S1). We find that pulse propagation velocities range from 0.04 m s^{-1} to 0.13 m s^{-1} (Text S4 and Figure S8 in Supporting Information S1). Remarkably, these observed pulse propagation velocities align closely with subglacial water flow velocities through an inefficient network of cavities as measured through dye experiments under alpine hard-bedded glaciers (Nienow et al., 1996). We also find that speed-up along-flow migration velocity is positively correlated with peak speed-up velocity (Figure 3d).

3.3. Model Predictions

The model successfully captures multi-decadal to seasonal sliding variations at the cavitometer site (Gilbert et al., 2022) and performs relatively well in explaining seasonal variations at the study site over the measurement period (Text S5 in Supporting Information S1). However, at the shorter timescales of the speed-up events, the model fails to reproduce the transient increases in horizontal velocity observed by GPS (dashed purple curve in Figure 2b), although it appropriately captures the amplitude and phasing of transient variations in vertical displacement (dashed purple curve in Figure 2c), given a realistic distance between bumps $l_r = 1$ m (see Section 2.3). We note that the modeled uplift between events 1 and 2 is driven by a 4-day melt period that did not trigger any visible uplift at the GPS stations (see Text S3 in Supporting Information S1). This could be due to the model's assumption of an instantaneous transfer of surface meltwater to the glacier base, leading to an overestimation of the water pressure increase in response to short melt events. The model's ability to reproduce the observed surface uplift, particularly its dependence on discharge (sea-green and olive lines in Figure 2e), gives confidence in its applicability to represent cavity dynamics at the short timescales of interest. However, the model's failure to reproduce the horizontal velocity while correctly modeling cavitation dynamics indicates that the friction law (Equation 2) does not apply to such short timescales of a few days. Using Equation 2, we find that θ must increase by 0.43 in order to explain the increase in horizontal velocity, implying a rate of change $\frac{d\theta}{dt} = 0.02\ \mathrm{h}^{-1}$, which is around 8 times greater than the modeled value of $0.0026\ \mathrm{hr}^{-1}$. To reach such a large value of $\frac{d\theta}{dt}$ using Equation 3, either a negative effective pressure less than −0.3 MPa or an exceptionally low value of l_r would be required. Both possibilities are unrealistic, suggesting that an additional contribution from effective pressure must be included in the friction law.

4. Discussion and Conclusion

4.1. Water Pressure as an Independent Driver of Basal Sliding Speed-Ups

Our observations indicate that effective pressure primarily drives basal sliding speed-ups. Borehole water pressure and basal velocity vary concomitantly (Figure 2b) and exhibit a similar trend across events (Figure 2d), while surface uplift, as at least partly inherited from changes in cavitation, is better correlated with water discharge than with basal velocity and pressure (Figure 2e). Maximum speed-up velocity is also positively correlated with the velocity at which speed-up and the underlying water flow migrate down-glacier (Figure 3d), giving further support that effective pressure primarily drives speed-ups: faster underlying water flow migration is expected to be driven by higher water pressure gradients and, thus, at a given distance from the glacier front, lower effective pressures. The absence of speed-up events in summer provides additional evidence that water pressure plays a key role. At this time of the year, the subglacial system is particularly efficient and thus prevents water pressure from rising sufficiently for speed-ups to occur.

As in previous studies (Anderson et al., 2004; Howat et al., 2008; Iken & Bindschadler, 1986; Mair et al., 2001; Vincent et al., 2022), bed separation inferred from surface uplift is highly uncertain, since a significant fraction of surface uplift may be caused by poorly constrained internal ice deformation (Figure 2c). Nevertheless, the order of magnitude of surface uplift is well captured by a cavitation law (Figure 2c) constrained a priori from long-term (seasonal to multi-decadal) observations of basal sliding (Gilbert et al., 2022). Even under the most conservative scenario of surface uplift being entirely due to cavitation, our modeling predictions show that increased cavitation is insufficient to explain the observed increase in basal sliding speed (Figure 2b). At the shorter timescales presently investigated, an additional contribution of effective pressure is to be invoked in order to explain the large changes observed in basal sliding speed.

4.2. Added Complexity From Water Pressure and Drainage Being Spatially Heterogeneous

We suggest that the deviations between the observed pressure and velocity time series highlight the limitation of using a local pressure measurement to infer larger-scale pressure-driven changes in sliding velocity. In particular, surface velocity rising before the water pressure can be explained by the pressure sensor connecting to the main hydrological network only after the event started, consistent with the pressure increase being nearly instantaneous and concomitant with a rapid uplift (Figure S4 in Supporting Information S1). The additional delay could also be due to the down-glacier propagating nature of speed-ups (Figure 3), in which case the velocity at a point initially increases as a result of changes in longitudinal stresses from basal pressure changes originating first higher up on the glacier rather than from local changes in basal water pressure. Speed-up events being systematically followed by a period of lower water pressure not affecting glacier velocity (Figure 2b) may be due to the pressure decrease being localized in the centerline of the glacier where the measurements are made and the drainage concentrates (Nanni et al., 2021), such that the associated frictional change may occur over an area too small to significantly change the overall basal friction. Good hydraulic connections created therein likely enhance conduit melting during speed-ups, but when the water supply stops, the efficient drainage of the centerline drives a water pressure drop that slowly rises again in response to the creep closure of the conduits formed during the rain events. This behavior is less likely to occur away from the central line because much less water is drained there (Hubbard et al., 1995). This heterogeneous distribution of the subglacial drainage system may also explain the phase shift between water pressure and horizontal velocity during event 3 (Figure 2b), for which the water pressure was in the process of recovering when the speed-up event occurred, whereas other events occurred under stable water pressure conditions (Gordon et al., 1998). In the following, we consider the borehole water pressure to represent the overall basal water pressure only between the peak pressure (shortly after the borehole connection is interpreted to occur), and the pre-event value (before water pressure is interpreted to be locally affected by enhanced drainage along the central line of the glacier).

4.3. A Generic Friction Law Applicable in Both the Transient and Steady-State Regimes

We propose to express τ_b as a function of U_b, θ, and N separately by extending Equation 2 with a direct dependency on N that only comes into play in the transient regime. Our new formulation retains the parameters from previous models (Gagliardini et al., 2007) without introducing new variables as:

$$\tau_b = \left((1-\theta)\frac{U_b}{A_s}\right)^{1/m} + f(\theta)\,(N - N^*(\theta, U_b)), \tag{4}$$

where $N^*(\theta,U_b)$ is the steady state effective pressure for a given cavity size θ and sliding speed U_b. $f(\theta)$ is a friction coefficient that describes the sensitivity of τ_b to effective pressure. $f(\theta)$ must be an increasing function of θ, since the effect of water pressure change into the force balance at the bed is a function of the area over which water pressure applies, which increases with θ. Under the assumption that the friction law follows a "regularized coulomb" friction law in the steady-state regime (Gagliardini et al., 2007; Helanow et al., 2021) we show in Appendix A that Equation 4 becomes:

$$\left(\frac{\tau_b}{CN}\right)^m = \left(((1-\theta)\chi)^{1/m}\left(1-\theta^{1-1/m}\right) + \theta\right)^m, \tag{5}$$

where $\chi = \frac{U_b}{(CN)^m A_s}$ with C a positive constant defined as $\tau_b(Ub \to \infty) = CN$. The evolution of θ in Equation 3 simplifies to:

$$\frac{d\theta}{dt} = \frac{1}{l_r}\left(U_b(1-\theta) - \theta A_s C^m |N|^{m-1} N\right). \tag{6}$$

Equations 5 and 6 constitute the generalized form of the "regularized coulomb" friction law for transient cavitation.

We attempt to constrain the friction term $f(\theta) = C\theta$ (see Appendix A) from our observations considering that basal shear stress is constant and the change in cavitation ratio has a negligible effect on friction during speed-up events, in which case we can express the surface velocity U_s from Equation 4 as:

$$U_s = \frac{A_s}{1-\theta}(\tau_b - C\theta(N - N^*))^m + U_d, \tag{7}$$

where U_d is the internal deformation velocity. The value τ_b (0.1 MPa), A_s (13,500 m a^{-1} MPa^{-3}), and θ (0.4) are known from the model in September 2019 and U_d is kept to its estimated value of 25 m a^{-1} (Section 2.3). Using the water pressure observations at the study site where ice thickness is 230 m, the term (N–N*) is estimated using water pressure before speed-up events as the steady-state water pressure setting $N^* = 0.52$ MPa. By fitting the velocity versus water pressure relationship observed in Figure 2d with Equation 7 we find $C\theta = 0.25$, which gives $C = 0.6$ using the value of $\theta = 0.4$ given by the model (Section 2.3). This value of C is higher than $C = 0.4$ found independently in Gimbert et al. (2021) based on multi-decadal observations and historical water pressure measurements. We note that our result is based on the assumption that the pressure measurement is perfectly connected to the main hydrologic network so that a change in pressure can be related to a change in sliding velocity. A lower rate of change of borehole water pressure compared to overall basal water pressure may result in a higher apparent value of $C\theta$. Investigating transient friction through theoretical considerations, as well as numerical experiments similar to those previously conducted in a steady state (Gagliardini et al., 2007), could help refine the presently proposed generalized friction law and the associated parameter values.

Appendix A: The Friction Law Derivation

To derive Equation 5, we consider that the steady state sliding law follows a "regularized coulomb" friction law (Helanow et al., 2021) such that in a steady state we have (using $q = 1$ in Gagliardini et al., 2007):

$$\left(\frac{\tau_b}{CN}\right)^m = \left(\frac{\chi}{1+\chi}\right) \tag{A1}$$

where $\chi = \frac{u_b}{(CN)^m A_s}$ with C a positive constant defined as $\tau_b(u_b \to \infty) = CN$. With this formulation, the equilibrium effective pressure N* can be linked to the cavitation ratio θ following Gilbert et al. (2022) as:

$$\theta = \left(\frac{U_b}{U_b + A_s(CN^*)^m}\right) \tag{A2}$$

For the limit case $\theta \to 0$, the friction law in Equation 4 must be independent of N, since no cavities exist, such that $f(\theta = 0) = 0$. For the limit case $\theta \to 1$ (or $U_b \to \infty$), friction must have the same dependency on N in both the steady and transient regimes, since cavity size no longer evolves in that case, such that we have:

$$\tau_b(U_b \to \infty) = CN + f(\theta = 1)(N - \tau_b/C) = CN \Rightarrow f(\theta = 1) = C$$

Assuming that a given pressure change occurring in cavitated parts of the bed increases τ_b linearly with θ, we have thus $f(\theta) = \theta C$. Substituting this expression into Equation 4 (also using Equation A2), we obtain the following generic law:

$$\tau_b = \left((1-\theta)\frac{U_b}{A_s}\right)^{1/m}\left(1 - \theta^{1-1/m}\right) + C\theta N \tag{A3}$$

This law is equivalent to the "regularized coulomb" steady friction law when U_b and N are at equilibrium with the cavity size and also $\forall (N, U_b)$ when $\theta \to 0$ or $\theta \to 1$. Equation A3 can equivalently be written as a function of χ as:

$$\left(\frac{\tau_b}{CN}\right)^m = \left(((1-\theta)\chi)^{1/m}\left(1 - \theta^{1-1/m}\right) + \theta\right)^m \tag{A4}$$

Data Availability Statement

The GNSS data used in this study are archived on the Oreme repository (Walpersdorf et al., 2023a, 2023b, 2023c). Other data are available on Zenodo (Togaibekov et al., 2023).

Acknowledgments
This work is part of the SAUSSURE project (ANR-18-CE01-0015-01) supported by the French National Research Agency (ANR). The GNSS equipment was provided by the French national mobile parc GPSmob. We thank all the people who conducted fieldwork, particularly Laurent Ott, Agnès Helmstetter, Christian Sue, and Martin Champon. We thank Christian Schoof for yielding the topic of transient friction in review rounds of a previous manuscript, Olivier Gagliardini and Christian Vincent for fruitful discussions, Luc Moreau for providing cavitometer data, and Luc Piard for conducting the drilling operations. We also thank two anonymous reviewers for their valuable comments.

References

Anderson, R. S., Anderson, S. P., MacGregor, K. R., Waddington, E. D., O'Neel, S., Riihimaki, C. A., & Loso, M. G. (2004). Strong feedbacks between hydrology and sliding of a small Alpine glacier. *Journal of Geophysical Research*, *109*(F3). https://doi.org/10.1029/2004JF000120

Chen, G. (1999). *GPS kinematic positioning for the airborne laser altimetry at Long Valley, California* (Thesis). Massachusetts Institute of Technology. Retrieved from https://dspace.mit.edu/handle/1721.1/9680

Das, S. B., Joughin, I., Behn, M. D., Howat, I. M., King, M. A., Lizarralde, D., & Bhatia, M. P. (2008). Fracture propagation to the base of the Greenland Ice Sheet during supraglacial lake drainage. *Science*, *320*(5877), 778–781. https://doi.org/10.1126/science.1153360

de Diego, G. G., Farrell, P. E., & Hewitt, I. J. (2022). Numerical approximation of viscous contact problems applied to glacial sliding. *Journal of Fluid Mechanics*, *938*, A21. https://doi.org/10.1017/jfm.2022.178

Fowler, A. C. (1986). A sliding law for glaciers of constant viscosity in the presence of subglacial cavitation. *Proceedings of the Royal Society of London. A. Mathematical and Physical Sciences*, *407*(1832), 147–170. https://doi.org/10.1098/rspa.1986.0090

Fowler, A. C. (1987). Sliding with cavity formation. *Journal of Glaciology*, *33*(115), 255–267. https://doi.org/10.3189/S0022143000008820

Fudge, T. J., Harper, J. T., Humphrey, N. F., & Pfeffer, W. T. (2009). Rapid glacier sliding, reverse ice motion and subglacial water pressure during an autumn rainstorm. *Annals of Glaciology*, *50*(52), 101–108. https://doi.org/10.3189/172756409789624247

Gagliardini, O., Cohen, D., Råback, P., & Zwinger, T. (2007). Finite-element modeling of subglacial cavities and related friction law. *Journal of Geophysical Research*, *112*(F2). https://doi.org/10.1029/2006JF000576

Gilbert, A., Gimbert, F., Gagliardini, O., & Vincent, C. (2023). Inferring the basal friction law from long term changes of glacier length, thickness and velocity on an Alpine Glacier. *Geophysical Research Letters*, *50*(16), e2023GL104503. https://doi.org/10.1029/2023GL104503

Gilbert, A., Gimbert, F., Thøgersen, K., Schuler, T. V., & Kääb, A. (2022). A consistent framework for coupling basal friction with subglacial hydrology on hard-bedded glaciers. *Geophysical Research Letters*, *49*(13), e2021GL097507. https://doi.org/10.1029/2021GL097507

Gimbert, F., Gilbert, A., Gagliardini, O., Vincent, C., & Moreau, L. (2021). Do existing theories explain seasonal to multi-decadal changes in glacier basal sliding speed? *Geophysical Research Letters*, *48*(15), e2021GL092858. https://doi.org/10.1029/2021GL092858

Gordon, S., Sharp, M., Hubbard, B., Smart, C., Ketterling, B., & Willis, I. (1998). Seasonal reorganization of subglacial drainage inferred from measurements in boreholes. *Hydrological Processes*, *12*(1), 105–133. https://doi.org/10.1002/(SICI)1099-1085(199801)12:1<105::AID-HYP566>3.0.CO;2-#

Harper, J. T., Humphrey, N. F., Pfeffer, W. T., & Lazar, B. (2007). Two modes of accelerated glacier sliding related to water. *Geophysical Research Letters*, *34*(12). https://doi.org/10.1029/2007GL030233

Helanow, C., Iverson, N. R., Woodard, J. B., & Zoet, L. K. (2021). A slip law for hard-bedded glaciers derived from observed bed topography. *Science Advances*, *7*(20), eabe7798. https://doi.org/10.1126/sciadv.abe7798

Herring, T. A., King, R. W., Floyd, M. A., & McClusky, S. C. (2018). *Introduction to GAMIT/GLOBK*. Massachusetts Institute of Technology.

Hooke, R. L., Calla, P., Holmlund, P., Nilsson, M., & Stroeven, A. (1989). A 3 year record of seasonal variations in surface velocity, StorglaciÄren, Sweden. *Journal of Glaciology*, *35*(120), 235–247. https://doi.org/10.3189/S0022143000004561

Howat, I. M., Tulaczyk, S., Waddington, E., & Björnsson, H. (2008). Dynamic controls on glacier basal motion inferred from surface ice motion. *Journal of Geophysical Research*, *113*(F3). https://doi.org/10.1029/2007JF000925

Hubbard, B. P., Sharp, M. J., Willis, I. C., Nielsen, M. K., & Smart, C. C. (1995). Borehole water-level variations and the structure of the subglacial hydrological system of Haut Glacier d'Arolla, Valais, Switzerland. *Journal of Glaciology*, *41*(139), 572–583. https://doi.org/10.3189/S0022143000034894

Iken, A. (1981). The effect of the subglacial water pressure on the sliding velocity of a glacier in an idealized numerical model. *Journal of Glaciology*, *27*(97), 407–421. https://doi.org/10.3189/S0022143000011448

Iken, A., & Bindschadler, R. A. (1986). Combined measurements of subglacial water pressure and surface velocity of Findelengletscher, Switzerland: Conclusions about drainage system and sliding mechanism. *Journal of Glaciology*, *32*(110), 101–119. https://doi.org/10.3189/S0022143000006936

Kamb, B. (1970). Sliding motion of glaciers: Theory and observation. *Reviews of Geophysics*, *8*(4), 673–728. https://doi.org/10.1029/RG008i004p00673

Lliboutry, L. (1958). Contribution a la theorie du frottement du glacier sur son lit. *Comptes Rendus Hebdomadaires des Seances de l'Academie des Sciences*, *247*, 318–320.

Lliboutry, L. (1968). General theory of subglacial cavitation and sliding of temperate glaciers. *Journal of Glaciology*, *7*(49), 21–58. https://doi.org/10.3189/S0022143000020396

Mair, D., Nienow, P., Willis, I., & Sharp, M. (2001). Spatial patterns of glacier motion during a high-velocity event: Haut Glacier d'Arolla, Switzerland. *Journal of Glaciology*, *47*(156), 9–20. https://doi.org/10.3189/172756501781832412

Mair, D., Sharp, M. J., & Willis, I. C. (2002). Evidence for basal cavity opening from analysis of surface uplift during a high-velocity event: Haut Glacier d'Arolla, Switzerland. *Journal of Glaciology*, *48*(161), 208–216. https://doi.org/10.3189/172756502781831502

Nanni, U., Gimbert, F., Roux, P., & Lecointre, A. (2021). Observing the subglacial hydrology network and its dynamics with a dense seismic array. *Proceedings of the National Academy of Sciences of the United States of America*, *118*(28), e2023757118. https://doi.org/10.1073/pnas.2023757118

Nienow, P. W., Sharp, M., & Willis, I. C. (1996). Velocity–discharge relationships derived from dye tracer experiments in glacial meltwaters: Implications for subglacial flow conditions. *Hydrological Processes*, *10*(10), 1411–1426. https://doi.org/10.1002/(SICI)1099-1085(199610)10:10<1411::AID-HYP470>3.0.CO;2-S

Nye, J. F. (1969). A calculation on the sliding of ice over a wavy surface using a Newtonian viscous approximation. *Proceedings of the Royal Society of London. A. Mathematical and Physical Sciences*, *311*(1506), 445–467. https://doi.org/10.1098/rspa.1969.0127

Nye, J. F. (1970). Glacier sliding without cavitation in a linear viscous approximation. *Proceedings of the Royal Society of London. A. Mathematical and Physical Sciences*, *315*(1522), 381–403. https://doi.org/10.1098/rspa.1970.0050

Schoof, C. (2005). The effect of cavitation on glacier sliding. *Proceedings of the Royal Society A: Mathematical, Physical and Engineering Sciences*, *461*(2055), 609–627. https://doi.org/10.1098/rspa.2004.1350

Sugiyama, S., & Gudmundsson, G. H. (2004). Short-term variations in glacier flow controlled by subglacial water pressure at Lauteraargletscher, Bernese Alps, Switzerland. *Journal of Glaciology*, *50*(170), 353–362. https://doi.org/10.3189/172756504781829846

Thøgersen, K., Gilbert, A., Schuler, T. V., & Malthe-Sørenssen, A. (2019). Rate-and-state friction explains glacier surge propagation. *Nature Communications*, *10*(1), 2823. Article 1. https://doi.org/10.1038/s41467-019-10506-4

Togaibekov, A., Gimbert, F., Gilbert, A., & Walpersdorf, A. (2023). Sliding velocity, water discharge, water pressure, and rainfall time series at Argentière Glacier between 2019 and 2021 [dataset]. *Zenodo*. https://doi.org/10.5281/zenodo.10419097

Tsai, V. C., Smith, L. C., Gardner, A. S., & Seroussi, H. (2022). A unified model for transient subglacial water pressure and basal sliding. *Journal of Glaciology*, *68*(268), 390–400. https://doi.org/10.1017/jog.2021.103

Vernay, M., Lafaysse, M., Monteiro, D., Hagenmuller, P., Nheili, R., Samacoïts, R., et al. (2022). The S2M meteorological and snow cover reanalysis over the French mountainous areas: Description and evaluation (1958–2021). *Earth System Science Data*, *14*(4), 1707–1733. https://doi.org/10.5194/essd-14-1707-2022

Vincent, C., Gilbert, A., Walpersdorf, A., Gimbert, F., Gagliardini, O., Jourdain, B., et al. (2022). Evidence of seasonal uplift in the Argentière Glacier (Mont Blanc Area, France). *Journal of Geophysical Research: Earth Surface*, *127*(7), e2021JF006454. https://doi.org/10.1029/2021JF006454

Vincent, C., & Moreau, L. (2016). Sliding velocity fluctuations and subglacial hydrology over the last two decades on Argentière glacier, Mont Blanc area. *Journal of Glaciology*, *62*(235), 805–815. https://doi.org/10.1017/jog.2016.35

Vivian, R., & Bocquet, G. (1973). Subglacial cavitation phenomena under the Glacier D'Argentière, Mont Blanc, France. *Journal of Glaciology*, *12*(66), 439–451. https://doi.org/10.3189/S0022143000031853

Walpersdorf, A., Ott, L., Helmstetter, A., Sue, C., Bouvier, J.-N., Champon, M., et al. (2023a). Epos-France—GPSMob data—Mission n° 19-050—Argentiere (2019)—2019-04-02/2020-01-01—7 points [Dataset]. *OSU OREME*. https://doi.org/10.15148/744be716-3207-4a26-bf7b-60b5fd304ffd

Walpersdorf, A., Ott, L., Helmstetter, A., Sue, C., Bouvier, J.-N., Champon, M., et al. (2023b). Epos-France—GPSMob data—Mission n° 20-021—Argentiere (2020)—2020-01-02/2021-01-01—13 points [Dataset]. *OSU OREME*. https://doi.org/10.15148/3fd58616-e0c4-4a7f-b2a9-7cf3db4933ba

Walpersdorf, A., Ott, L., Helmstetter, A., Sue, C., Bouvier, J.-N., Champon, M., et al. (2023c). Epos-France—GPSMob data—Mission n° 21-028—Argentiere (2021)—2021-01-02/2021-12-31—13 points [Dataset]. *OSU OREME*. https://doi.org/10.15148/ff97d3bb-0db2-4d21-8abe-999a7c2565cd

Weertman, J. (1957). On the sliding of glaciers. *Journal of Glaciology*, *3*(21), 33–38. https://doi.org/10.3189/S0022143000024709